Reduced Order Equivalent Circuit Model of Series Resonant Converter Considering the Interaction Between Resonant Elements

Xin Li, *Member, IEEE*, Jianing Li, Peili Yuan, Jiangfeng Wang, *Member, IEEE*, Wu Chen, *Senior Member, IEEE*, Shiqi Kan, *Member, IEEE*, and Jian Ai

***Abstract*—The high order and complex structure of the resonant converter small-signal equivalent circuit prevents it from providing plentiful physical insights. It is of significance to obtain a more accessible and simpler equivalent circuit. This article investigates the order reduction and approximation of the equivalent circuit of the series resonant converter (SRC). It is shown that there is a close interaction between the resonant inductor model and the resonant capacitor model that must be carefully considered when conducting approximation. Using this methodology, a concise third-order equivalent circuit of the SRC is proposed. This equivalent circuit can capture the beat frequency dynamic very accurately. Moreover, it eliminates the phase error that exists in the existing models, ensuring better stability when designing the closed loop system. Finally, the experimental results verify the validity of the equivalent circuit model.**

***Index Terms*—Equivalent circuit, interaction, order reduction, series resonant converter (SRC).**

I. Introduction

DUE to the advantages of high switching frequency, high efficiency, and high-power density, the resonant converter has prevailed in many applications, such as data center power supply, electric vehicle charger, and wireless power transfer, among others [1], [2], [3], [4].

To satisfy the dynamic and stability specifications, it is necessary to establish a small-signal model that can well describe the converter. Several methods have been presented to model the resonant converter. Discrete-time models or the sample-data models were proposed in [5], [6], but the modeling process is complex and shows a limited physical insight, which restricts its application. A small-signal model based on state plane analysis and *dq*-transformation was proposed in [7], [8], but this technique is mainly applicable in two-element resonant tank. Some modeling methods that combine time and frequency domain analyses are easy to understand and implement, and they have been prevailing over the years, for example, the dynamic phasor transformation technique [9], [10], the generalized state space averaging [11], [12] and the extended describing function method [13], [14].

The derived models in [5], [6], [7], [8], [9], [10], [11], [12], [13], and [14] are usually presented in the form of state-space representation, from which the numerical or symbolic transfer functions can be extracted, but these models provide few physical insights. Comparatively speaking, an equivalent circuit of the model is a clearer and more flexible format to reveal more physical insights. In [15], the equivalent circuit model of the resonant converter in complex domain was proposed, where the variables are expressed with vectors, which is very abstract to comprehend. By separating the complex-domain circuit into sine part and cosine part, a time-domain equivalent circuit that is suitable for simulation was obtained [16].

Note that the equivalent circuit in [15] and [16] is essentially equivalent to the state-space representation, and thus has excellent accuracy up to the switching frequency. However, it comes with the high-order and complex structure, making it too complicated to be of much analytical usefulness. In fact, such wide accuracy is unnecessary in most closed loop design, where the bandwidth is usually much lower than the switching freuqency. To this end, some order reduction and approximation approaches were proposed to obtain more concise equivalent circuits. As the simplest resonant converter, the series resonant converter (SRC) has long been a research object of this issue. In [17], a two-port y parameter equivalent circuit model of SRC was proposed. This equivalent circuit introduces a series of transfer functions to represent the dependent sources and the impedances, yet it is not in the form of a standard linear time-invariant circuit and bring difficulty to understand and use. In [18], the small-signal equivalent circuit of the SRC was approximated to be a first-order circuit when the switching frequency approaches the resonant frequency, and a second-order circuit when the switching frequency deviates from the resonant frequency. This equivalent circuit is effective in capturing the very low frequency

Received 11 July 2025; revised 13 November 2025; accepted 16 December 2025. Date of publication 31 December 2025; date of current version 20 March 2026. This work supported in part by the National Natural Science Foundation of China under Grant 52307196, in part by the Natural Science Foundation of Jiangsu Province under Grant BK20230850, and in part by the Zhishan Young Scholar Support Program of Southeast University under Grant 3216002505A2. Recommended for publication by Associate Editor B. Singh. *(Corresponding author: Jian Ai.)*

Xin Li, Jianing Li, Peili Yuan, Jiangfeng Wang, and Wu Chen are with the School of Electrical Engineering, Southeast University, Nanjing 210096, China (e-mail: li-xin@seu.edu.cn; 220243073@seu.edu.cn; 220243087@seu.edu.cn; jfwang@seu.edu.cn; chenwu@seu.edu.cn).

Shiqi Kan is with Yangzhou University, Yangzhou 225000, China (e-mail: kanshiqi@yzu.edu.cn).

Jian Ai is with Jiangnan University, Wuxi 214122, China (e-mail: jianai0204@jiangnan.edu.cn).

Color versions of one or more figures in this article are available at https://doi.org/10.1109/TPEL.2025.3649643.

Digital Object Identifier 10.1109/TPEL.2025.3649643

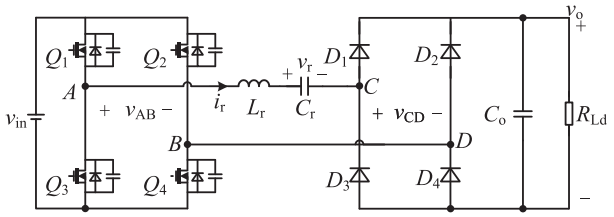

Fig. 1. Topology of the series resonant converter.

characteristic of the SRC, but fails in relative high frequency range, e.g., predicting the beat frequency dynamics as reported in [19]. The beat frequency dynamic refers to the dynamic issue caused by a double pole located at the difference of the switching frequency and the resonant frequency. Accurately predicting the beat frequency dynamics is crucial for closed-loop stability enhancing and preventing oscillations in the system. In [20], an approximate third-order equivalent circuit of the SRC was proposed, where the resonant capacitor was approximated to be an inductor in lower frequency range. The equivalent circuit in [20] has very concise form and shows fruitful physical insights. However, although accurate in most cases, this article finds the third-order equivalent circuit in [20] has some problems in certain circumstances. For example, the beat frequency double pole it predicts has a deviation from the actual position when the switching frequency is far away from the resonant frequency; and the predicted phase may be much higher than the actual phase in high frequency range, posing a risk of system instability when the bandwidth of the DABSRC closed loop system is high. Other reduced-order models for SRC, as given in [21] and [22] also fail to accurately predict the beat frequency pole, and the phase response also exhibits deviations in the high-frequency range.

This article investigates the reason for the inaccuracy of the existing reduced order equivalent circuits of SRC and re-derives a more accurate third-order equivalent circuit without increasing complexity.

The rest of this article is organized as follows. In Section II, the existing accurate and the approximate third-order equivalent circuit of SRC are reviewed. In Section III, the equivalent circuit of the resonant network considering the interaction between the resonant elements is derived. In Section IV, the approximation of the switching frequency-controlled sources in the equivalent circuit is conducted. Combining the results in Sections III and IV, a decoupled third-order equivalent circuit of SRC is proposed in Section V. Section VI has a discussion of the proposed equivalent circuit. Section VII provides the experimental data to verify the validity of the proposed equivalent circuit. Finally, Section VIII concludes this article.

II. Review of the Accurate and Approximated Equivalent Circuit of the SRC

Fig. 1 is the topology of SRC. The input (output) voltage is $v_{\rm in}(v_o)$. The resonant tank is composed of the resonant inductor L_r, and the resonant capacitor C_r. vr and ir are the resonant capacitor voltage and the resonant inductor current, respectively.

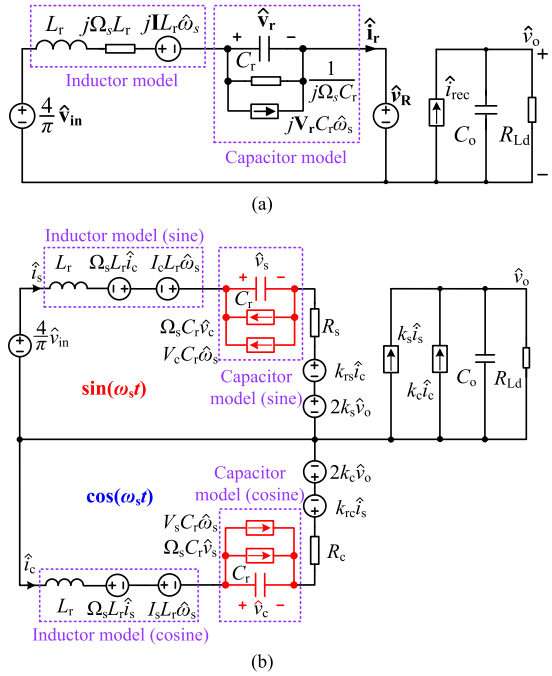

Fig. 2. Accurate small-signal equivalent circuit of SRC in (a) complex domain and (b) time domain.

Co is the output filter capacitor, $R_{\rm Ld}$ is the load resistor. The switching (angular) frequency is $f_s(\omega_s)$. The resonant (angular) frequency is f_r (ω_r), Fig. 2(a) is the small-signal equivalent circuit in complex domain proposed in [15], where $\mathbf{V_r}$ and $\mathbf{I_r}$ are the vectors of the resonant capacitor voltage and the resonant inductor current in the steady state. $\hat{\mathbf{v}}_\mathbf{r}$ and $\hat{\mathbf{i}}_\mathrm{r}$ are their corresponding small-signal vectors. Please note that the symbols with the first letter in capital represent the steady-state components of the variables, while the variables with a cap represent the small-signal components in this article. Observed from Fig. 2(a), the resonant inductor model is comprised of the inductor L_r, the complex impedance $j\Omega_\mathrm{s}L_r$, and a frequency-controlled voltage source $j\mathbf{I_r}L_\mathrm{r}\hat{\omega}_s$, where Ω_s is switching angular frequency in steady state. The resonant capacitor model is comprised of the capacitor C_r, the complex impedance $1/j\Omega_sC_r$, and a frequency controlled current source $j\mathbf{V_r}C_\mathrm{r}\hat{\omega}_\mathrm{s}$.

By separating the complex-domain circuit into sine part and cosine part, a time-domain equivalent circuit that is suitable for simulation is presented in Fig. 2(b) $\hat{v}_{\mathrm{s(c)}}$, $\hat{i}_{\mathrm{s(c)}}$ are the sine (cosine) components of $\hat{\mathbf{v}}_\mathbf{r}$ and $\hat{\mathbf{i}}_\mathrm{r}$. k_{rs}, k_{rc}, k_s, k_c, R_s, R_c, V_s, V_c, I_s, and I_c are the coefficients of the dependent sources, whose expressions are provided in the Appendix. From Fig. 2(b), we can find the equivalent circuit is a fifth order system and has complicated structure, making it very hard to be of much analytical usefulness.

Tian et al. [20] proposed a low-frequency third-order approximate equivalent circuit by simplifying the capacitor model in Fig. 2, which will be reviewed below.

In the freuqency range far below the steady-state switching (angular) frequency $F_s(\Omega_s)$, we have $|s^2| << \Omega_s^2$, therefore the parallel impedance of sC_r and $1/j\Omega_sC_r$ in Fig. 2(a) are

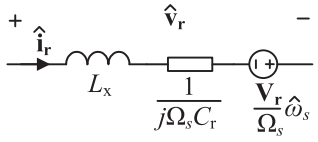

Fig. 3. Approximated resonant capacitor model proposed in [20].

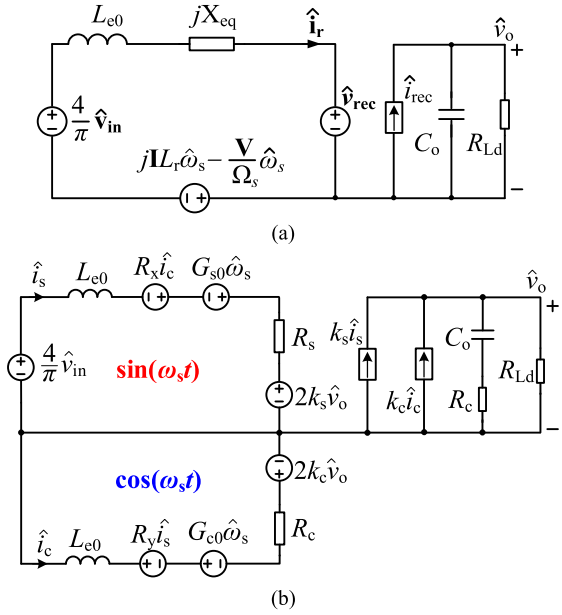

Fig. 4. Approximated third-order small-signal circuit of SRC proposed in [20] in (a) the complex domain and (b) the time domain.

approximated as

$$\frac{\hat{\mathbf{v}}_r}{\hat{\mathbf{i}}_r} = \frac{1}{sC_r + j\Omega_s C_r} = \frac{1-\frac{s}{j\Omega_s}}{j\Omega_s C_r\left(1+\frac{s^2}{\Omega_s^2}\right)} \approx \frac{s}{\Omega_s^2 C_r} + \frac{1}{j\Omega_s C_r}. \tag{1}$$

Moreover, using Thevenin theorem, the frequency-controlled current source $j\mathbf{V_r}C_\mathrm{r}\hat{\omega}_\mathrm{s}$ is converted to a voltage source in low frequency range, i.e.,

$$\frac{1}{sC_r + j\Omega_s C_r} j\mathbf{V}_r C_r \hat{\omega}_s \approx \frac{\mathbf{V}_r \hat{\omega}_s}{\Omega_s}. \tag{2}$$

Using (1) and (2), the resonant capacitor model is approximated to be Fig. 3. Obviously, the capacitor behaves like an inductor in the low frequency range.

Replacing the resonant capacitor model with Fig. 3 leads to a third-order circuit of SRC, as shown in Fig. 4(a), where the equivalent impedance of the resonant inductor and resonant capacitor, denoted as $Z_{\mathrm{LC\_aprx0}}(s)$, is

$$\mathbf{Z}_{\mathrm{LC\_aprx0}}(s) \approx sL_{e0} + jX_{\mathrm{eq}}. \tag{3}$$

The equivalent inductor L_{e0} is expressed as

$$L_{e0} = L_r\left(1+\frac{\Omega_r^2}{\Omega_s^2}\right) \tag{4}$$

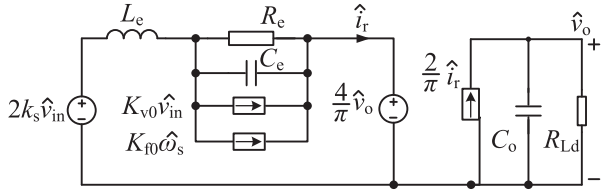

Fig. 5. Deccoupled third-order small-signal circuit of SRC in [20].

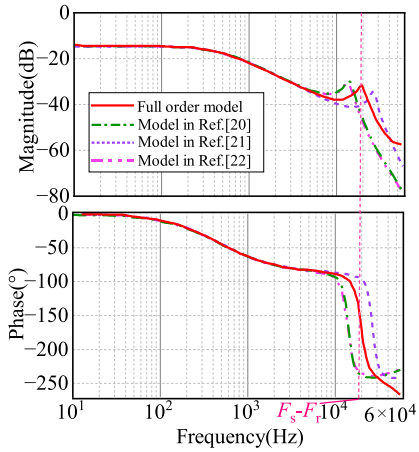

Fig. 6. Bode plot of $Gvg(s)$ from the full-order SRC model and the existing three reduced third-order models in [20], [21], [22] when $Fs = 0.6\ Fr$, $Q = 4.972$ with the circuit parameters in Table I.

where Ω_r is the resonant angular frequency of L_r and C_r, expressed as

$$\Omega_r = \frac{1}{\sqrt{L_r C_r}}. \tag{5}$$

X_{eq} is

$$X_{\mathrm{eq}} = \Omega_s L_r - \frac{1}{\Omega_s C_r}. \tag{6}$$

The corresponding time-domain representation of Fig. 4(a) is shown in Fig. 4(b), where the coefficients of the dependent sources, R_x, R_y, G_{s0}, and G_{c0} are given in the Appendix. In Fig. 4(b), the dependent voltage sources $R_\mathrm{x}\hat{i}_\mathrm{c}$ and $R_\mathrm{y}\hat{i}_\mathrm{s}$ represent the coupling between the sine part and cosine part.

To better yield the physical insights, a decoupled third-order equivalent circuit in time domain was further proposed in [20], as illustrated in Fig. 5, wherse $\hat{i}_\mathrm{c}$ and $\hat{i}_\mathrm{s}$ are merged into the actual resonant current $\hat{i}_\mathrm{r}$, and the dependent sources representing the coupling are all eliminated. The coefficients K_{v0}, K_{f0} are given in the Appendix. Obviously, Fig. 5 is more concise and useful than Fig. 4.

It is worth noting that there are other reduced-order models reported for SRC in [21] and [22]. Vyapari et al. [21] is essentially equivalent to [20], while Chacko and Lakshminarasamma [22] also adopted (4) to simplify the capacitor. In addition, it uses the assumption $|s| << \Omega_\mathrm{s}$ for approximation, which leads to different transfer functions. Their final bode plots (see Figs. 6 and 7) fail to accurately predict the beat frequency double pole. Furthermore, the phase response of them also exhibits deviations in the high-frequency range.

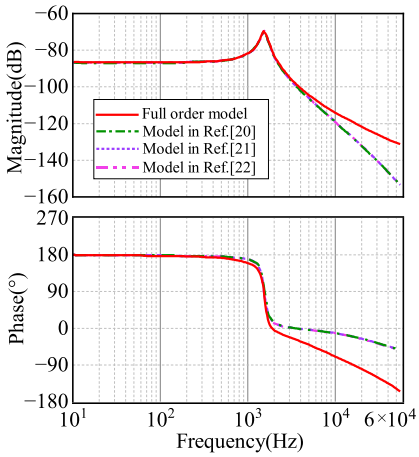

Fig. 7. Bode plot of $Gvf(s)$ from the full-order SRC model and the three existing reduced third-order models when $Fs = 1.05$ Fr, $Q = 0.642$ with the circuit parameters in Table I.

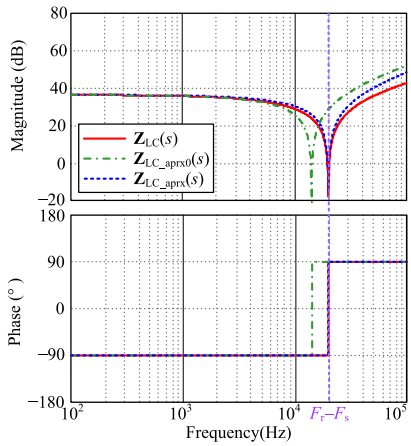

Fig. 8. Comparison of lying the numerator and denomi$_{LC}(s)$ by different equivalent when $\Omega s = 0.6\Omega r$.

III. Equivalent Circuit of the Impedance Network

Recall the derivation of the third-order equivalent circuit in [20], the approximation was conducted only for the resonant capacitor model. However, in fact, the equivalent circuit is determined jointly by the inductor model and the capacitor model. There is a close interaction between the resonant inductor model and the resonant capacitor model. The approximated capacitor model in [20] is valid for itself, but might fail when applied to the entire circuit. This article will derive an equivalent circuit of the SRC with the consideration of the interaction between the resonant elements. The approximation of the passive impedance network will be presented in this section.

The impedance of the inductor and capacitor series network in Fig. 2(a) can be expressed as

$$\begin{aligned}\mathbf{Z}_{\mathrm{LC}}(s) &= sL_r + j\Omega_s L_r + \frac{1}{sC_r + j\Omega_s C_r} \\ &= \frac{(sL_r + j\Omega_s L_r)(sC_r + j\Omega_s C_r) + 1}{j\Omega_s C_r\left(1 + \frac{s}{j\Omega_s}\right)}.\end{aligned} \tag{7}$$

Multiplying the numerator and denominator of $\mathbf{Z}_{\mathrm{LC}}(s)$ by $1-s/ja\Omega_s$ at the same time, $\mathbf{Z}_{\mathrm{LC}}(s)$ becomes

$$\mathbf{Z}_{\mathrm{LC}}(s) = \frac{[(sL_r + j\Omega_s L_r)(sC_r + j\Omega_s C_r) + 1]\left(1 - \frac{s}{ja\Omega_s}\right)}{j\Omega_s C_r\left(1 + \frac{s}{j\Omega_s}\right)\left(1 - \frac{s}{ja\Omega_s}\right)} \tag{8}$$

where a can be any real number pending determined.

Expanding (8) leads to

$$\begin{aligned}\mathbf{Z}_{\mathrm{LC}}(s) = &\frac{j\left(\Omega_s L_r - \frac{1}{\Omega_s C_r}\right)}{1 + \frac{a-1}{a}\frac{s}{j\Omega_s} + \frac{s^2}{a\Omega_s^2}} \\ &+ \frac{sL_r\left[2 - \frac{1}{a} + \frac{1}{a\Omega_s^2 L_r C_r} + \left(1 - \frac{2}{a}\right)\frac{s}{j\Omega_s} + \frac{s^2}{a\Omega_s^2}\right]}{1 + \frac{a-1}{a}\frac{s}{j\Omega_s} + \frac{s^2}{a\Omega_s^2}}.\end{aligned} \tag{9}$$

Note the denominator of (9) is a second-order differentiation element, in which the corner frequencies of s and s^2 terms are $|\frac{a}{a-1}|\Omega_s$, $\sqrt{|a|}\Omega_s$, respectively. When $a>1$, the corner frequencies of s and s^2 terms are higher than Ω_s, thus the following approximation holds true in the frequency range $|s| << \Omega_s$,

$$1 + \left(1 - \frac{1}{a}\right)\frac{s}{j\Omega_s} + \frac{s^2}{a\Omega_s^2} \approx 1. \tag{10}$$

Similarly, the corner frequencies of s and s^2 terms of the second-order differentiation element in the numerator are also higher than Ω_s when $a>1$, therefore we have

$$\begin{aligned}&2 - \frac{1}{a} + \frac{1}{a\Omega_s^2 L_r C_r} + \left(1 - \frac{2}{a}\right)\frac{s}{j\Omega_s} + \frac{s^2}{a\Omega_s^2} \\ &\quad\approx 2 - \frac{1}{a} + \frac{1}{a\Omega_s^2 L_r C_r}.\end{aligned} \tag{11}$$

With (10) and (11), $\mathbf{Z}_{\mathrm{LC}}(s)$ is approximated to be $\mathbf{Z}_{\mathrm{LC\_aprx}}(s)$ when $|s| << \Omega_s$, which is expressed as

$$\mathbf{Z}_{\mathrm{LC\_aprx}}(s) \approx sL_r\left(2 - \frac{1}{a} + \frac{1}{a\Omega_s^2 L_r C_r}\right) + jX_{\mathrm{eq}}. \tag{12}$$

Evidently, the passive impedance network exhibits inductive characteristic. The value of equivalent inductor depends on the choice of a.

Observing the curve of $\mathbf{Z}_{\mathrm{LC}}$ in Fig. 8, it is found $\mathbf{Z}_{\mathrm{LC}}$ has an impedance valley, by letting $|\mathbf{Z}_{\mathrm{LC}}(s)| = 0$, the corresponding frequency of which can be solved as

$$s = j\left(\Omega_r - \Omega_s\right). \tag{13}$$

To ensure that the models before and after approximation have high consistency, $\mathbf{Z}_{\mathrm{LC\_aprx}}(s)$ should also be zero at $s = j(\Omega_r - \Omega_s)$, i.e.,

$$\begin{aligned}&|\mathbf{Z}_{\mathrm{LC\_aprx}}[j\left(\Omega_r - \Omega_s\right)]| \\ &\quad\approx \left|\left(\Omega_r - \Omega_s\right)L_r\left(2 - \frac{1}{a} + \frac{1}{a\Omega_s^2 L_r C_r}\right) + X_{\mathrm{eq}}\right|. \\ &\quad= 0\end{aligned} \tag{14}$$

from which, a is solved to be

$$a = 1 + \frac{\Omega_r}{\Omega_s}. \tag{15}$$

Substituting (15) into (12), the final expression of $\mathbf{Z}_{\mathrm{LC\cdot aprx}}(s)$ is

$$\mathbf{Z}_{\mathrm{LC\_aprx}}(s) \approx sL_r\left(1 + \frac{\Omega_r}{\Omega_s}\right) + jX_{\mathrm{eq}}. \tag{16}$$

The equivalent inductor, denoted as L_e, is expressed as

$$L_e = L_r\left(1 + \frac{\Omega_r}{\Omega_s}\right). \tag{17}$$

Obviously, the proposed L_e here is different from L_{e0} in [20] except when $\Omega_s = \Omega_r$. Fig. 8 illustrates both the curves of $\mathbf{Z}_{\mathrm{LC\cdot aprx}}(s)$ and $\mathbf{Z}_{\mathrm{LC\cdot aprx0}}(s)$. It evidently shows that $\mathbf{Z}_{\mathrm{LC\cdot aprx}}(s)$ has a better agreement with $\mathbf{Z}_{\mathrm{LC}}(s)$ than $\mathbf{Z}_{\mathrm{LC\cdot aprx0}}(s)$, especially at and after the impedance valley.

IV. Equivalent Circuit of the Frequency-Controlled Sources

According to Fig. 2, the complete frequency- controlled source is superimposed of that from the resonant inductor model and that from the resonant capacitor model. Numerous simulation and experiment results show the interaction between the inductor and capacitor has no fixed varying pattern. Due to this reason, this article intends to approximate Fig. 2 from the accurate state equations to minimize the error. Solving the accurate fifth-order state equations in Fig. 2 will be very complicated and tedious. To avoid this problem, we assume $\hat{v}_{\mathrm{in}}$ and $\hat{v}_{\mathrm{o}}$ to be zero with the aim of obtaining the simplest possible state equation about the inductor current under the perturbation of $\hat{\omega}_{\mathrm{s}}$. Considering this, the resonant voltage equations from Fig. 2(b) are

$$\begin{cases} \frac{d\hat{v}_s}{dt} = \frac{\hat{i}_s}{C_r} + \Omega_s\hat{v}_c + V_c\hat{\omega}_s \\ \frac{d\hat{v}_c}{dt} = \frac{\hat{i}_c}{C_r} - \Omega_s\hat{v}_s - V_s\hat{\omega}_s \end{cases}. \tag{18}$$

Using Laplace transform, (18) is solved to be

$$\begin{bmatrix}\hat{v}_s \\ \hat{v}_c\end{bmatrix} = \frac{1}{C_r}\frac{1}{s^2+\Omega_s^2}\begin{bmatrix}s\hat{i}_s + \Omega_s\hat{i}_c \\ -\Omega_s\hat{i}_s + s\hat{i}_c\end{bmatrix} + \frac{1}{s^2+\Omega_s^2}\begin{bmatrix}sV_c - V_s\Omega_s \\ -V_c\Omega_s - sV_s\end{bmatrix}\hat{\omega}_{\mathrm{s}}. \tag{19}$$

Similarly, state equations of the resonant currents are

$$\begin{cases} \frac{d\hat{i}_s}{dt} = -\frac{R_s}{L_r}\hat{i}_s + \left(\Omega_s - \frac{k_{rs}}{L_r}\right)\hat{i}_c - \frac{1}{L_r}\hat{v}_s + I_c\hat{\omega}_s \\ \frac{d\hat{i}_c}{dt} = -\left(\Omega_s + \frac{k_{rc}}{L_r}\right)\hat{i}_s - \frac{R_c}{L_r}\hat{i}_c - \frac{1}{L_r}\hat{v}_c - I_s\hat{\omega}_s \end{cases} \tag{20}$$

which can be written as

$$\begin{bmatrix} sL_r + R_s & -L_r\Omega_s + k_{rs} \\ L_r\Omega_s + k_{rc} & sL_r + R_c \end{bmatrix}\begin{bmatrix}\hat{i}_s \\ \hat{i}_c\end{bmatrix} = -\begin{bmatrix}\hat{v}_s \\ \hat{v}_c\end{bmatrix} + \begin{bmatrix}L_rI_c \\ -L_rI_s\end{bmatrix}\hat{\omega}_s. \tag{21}$$

Substituting (19) into (20), and after rearrangement, we can get the state equations without resonant voltages,

$$\begin{bmatrix} sL_r + \frac{1}{C_r}\frac{s}{s^2+\Omega_s^2} + R_s & -L_r\Omega_s + \frac{1}{C_r}\frac{\Omega_s}{s^2+\Omega_s^2} + k_{rs} \\ L_r\Omega_s - \frac{1}{C_r}\frac{\Omega_s}{s^2+\Omega_s^2} + k_{rc} & sL_r + \frac{1}{C_r}\frac{s}{s^2+\Omega_s^2} + R_c \end{bmatrix}\begin{bmatrix}\hat{i}_s \\ \hat{i}_c\end{bmatrix} = \begin{bmatrix} L_rI_c - \frac{sV_c - \Omega_sV_s}{s^2+\Omega_s^2} \\ -L_rI_s + \frac{sV_s + \Omega_sV_c}{s^2+\Omega_s^2}\end{bmatrix}\hat{\omega}_{\mathrm{s}}. \tag{22}$$

The state matrix in (22) is denoted as

$$\mathbf{A} = \begin{bmatrix} sL_r + \frac{1}{C_r}\frac{s}{s^2+\Omega_s^2} + R_s & -L_r\Omega_s + \frac{1}{C_r}\frac{\Omega_s}{s^2+\Omega_s^2} + k_{rs} \\ L_r\Omega_s - \frac{1}{C_r}\frac{\Omega_s}{s^2+\Omega_s^2} + k_{rc} & sL_r + \frac{1}{C_r}\frac{s}{s^2+\Omega_s^2} + R_c \end{bmatrix}. \tag{23}$$

Solving (22), we have

$$\begin{bmatrix}\hat{i}_s \\ \hat{i}_c\end{bmatrix} = \mathbf{A}^{-1}\begin{bmatrix} L_rI_c - \frac{sV_c - \Omega_sV_s}{s^2+\Omega_s^2} \\ -L_rI_s + \frac{sV_s + \Omega_sV_c}{s^2+\Omega_s^2}\end{bmatrix}\hat{\omega}_s. \tag{24}$$

The actual resonant current $\hat{i}_{\mathrm{r}}$ is the superposition of $\hat{i}_{\mathrm{s}}$ and $\hat{i}_{\mathrm{c}}$, which is expressed to be [15]

$$\hat{i}_r = \frac{\pi}{2}k_s\hat{i}_s + \frac{\pi}{2}k_c\hat{i}_c. \tag{25}$$

Substituting (23) into (24), and simplifying it, the expression of $\hat{i}_{\mathrm{r}}$ is found to be

$$\hat{i}_r = \frac{1}{|\mathbf{A}|}\frac{4}{\pi}\frac{V_{\mathrm{in}}}{C_r^2\Omega_s\sqrt{R_{\mathrm{eq}}^2 + X_{\mathrm{eq}}^2}} \cdot \frac{\left(\frac{s^2}{\Omega_r^2} + 1 + \frac{\Omega_s^2}{\Omega_r^2}\right)\left(1 - \frac{\Omega_s^2}{\Omega_r^2}\right) + sR_{\mathrm{eq}}C_r}{s^2 + \Omega_s^2}\hat{\omega}_s \tag{26}$$

where R_{eq} is the equivalent load resistor and is expressed as

$$R_{\mathrm{eq}} = \frac{8}{\pi^2}R_{\mathrm{Ld}}. \tag{27}$$

When $|s| << \Omega_{\mathrm{s}}$, $\hat{i}_{\mathrm{r}}$ is approximated to be

$$\hat{i}_r \approx \frac{1}{|\mathbf{A}|}\frac{4}{\pi}\frac{V_{\mathrm{in}}}{\sqrt{R_{\mathrm{eq}}^2 + X_{\mathrm{eq}}^2}}\frac{1 - \frac{\Omega_s^4}{\Omega_r^4} + sR_{\mathrm{eq}}C_r}{C_r^2\Omega_s}\hat{\omega}_s. \tag{28}$$

In Section III, the passive impedance network has been approximated. Therefore, the equivalent circuit of SRC can be depicted in the form of Fig. 9 , where G_s, G_c are coefficients of the frequency-controlled voltage sources pending to be settled. In order to minimize the error of the reduced order equivalent circuit, the expression of $\hat{i}_{\mathrm{r}}$ derived from Fig. 2 should be as consistent as possible with (28).

Similarly, setting $\hat{v}_{\mathrm{in}}$ and $\hat{v}_{\mathrm{o}}$ to be zero in Fig. 9, the state equations of the resonant currents are

$$\begin{cases} \frac{d\hat{i}_s}{dt} = -\frac{R_s}{L_e}\hat{i}_s + \frac{R_x}{L_e}\hat{i}_c + \frac{G_s}{L_e}\hat{\omega}_s \\ \frac{d\hat{i}_c}{dt} = -\frac{R_y}{L_e}\hat{i}_s - \frac{R_c}{L_e}\hat{i}_c - \frac{G_c}{L_e}\hat{\omega}_s \end{cases}. \tag{29}$$

Using Laplace transform, we have

$$\begin{bmatrix} sL_e + R_s & -R_x \\ R_y & sL_e + R_c \end{bmatrix}\begin{bmatrix}\hat{i}_s \\ \hat{i}_c\end{bmatrix} = \begin{bmatrix}G_s \\ -G_c\end{bmatrix}\hat{\omega}_s. \tag{30}$$

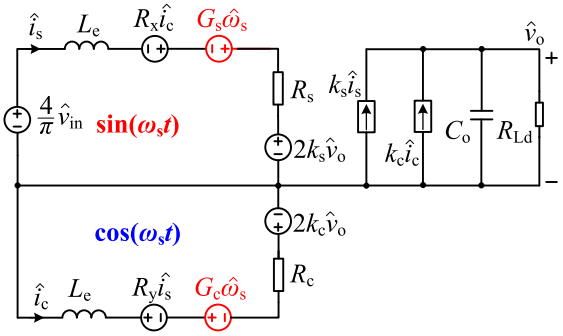

Fig. 9. Proposed third-order small-signal circuit of SRC.

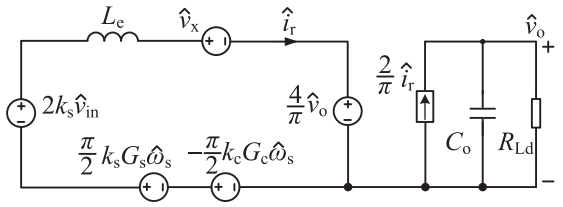

Fig. 10. Equivalent circuit of SRC with the dependent voltage source $\hat{v}_x$.

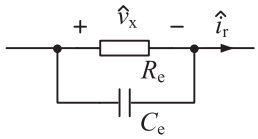

Fig. 11. Equivalent impedance representing the relationship between $\hat{v}_x$ caused $\hat{i}_r$.

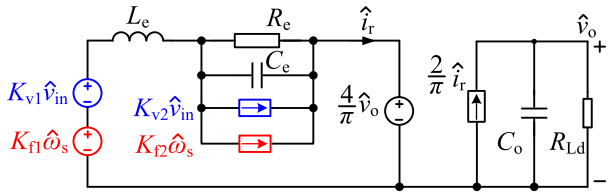

Fig. 12. Final form of the proposed third-order equivalent circuit of SRC.

TABLE I
PARAMETERS OF THE DABSRC

Parameters	Values	Parameters	Values
V_{in}	30 V	C_r	51 nF
f_r	49.96 kHz	C_o	22 μF
L_r	199 μH	R_{Ld}	10-120 Ω

Defining the sate matrix in (30) as

$$\mathbf{A}_{\text{aprx}} = \begin{bmatrix} sL_e + R_s & -R_x \\ R_y & sL_e + R_c \end{bmatrix}. \tag{31}$$

The deduced approximate $\hat{i}_r$ is expressed as

$$\hat{i}_r = \frac{1}{|\mathbf{A}_{\text{aprx}}|} \frac{G_s\left(R_{\text{eq}}^2 + X_{\text{eq}}^2\right) + sL_e\left(G_sR_{\text{eq}} + G_cX_{\text{eq}}\right)}{\sqrt{R_{\text{eq}}^2 + X_{\text{eq}}^2}} \hat{\omega}_s. \tag{32}$$

Comparing (28) and (32), $|\mathbf{A}|$ can be approximated with $|\mathbf{A}_{\text{aprx}}|$, i.e.,

$$|\mathbf{A}| \approx |\mathbf{A}_{\text{aprx}}| = s^2L_e^2 + sL_eR_{\text{eq}} + X_{\text{eq}}^2. \tag{33}$$

The numerators of (28) and (32) should also be equal, therefore

$$\frac{4V_{\text{in}}}{\pi} \frac{1 - \frac{\Omega_s^4}{\Omega_r^4} + sR_{\text{eq}}C_r}{C_r^2\Omega_s} = G_s\left(R_{\text{eq}}^2 + X_{\text{eq}}^2\right) + sL_e\left(G_sR_{\text{eq}} + G_cX_{\text{eq}}\right) \tag{34}$$

from which, G_s and G_c are solved to be

$$G_s = -\frac{4V_{\text{in}}X_{\text{eq}}\left(1 + \Omega_s^2L_rC_r\right)}{\pi C_r\Omega_s^2\left(R_{\text{eq}}^2 + X_{\text{eq}}^2\right)} \tag{35}$$

$$G_c = \frac{4V_{\text{in}}R_{\text{eq}}\left(1 + \Omega_s^2L_rC_r\right)}{\pi C_r\Omega_s^2\left(R_{\text{eq}}^2 + X_{\text{eq}}^2\right)} + \frac{4V_{\text{in}}R_{\text{eq}}}{\pi L_eC_rX_{\text{eq}}\Omega_s^3}. \tag{36}$$

Compared with the derived G_{s0} and G_{c0} by [20], the following relationship is found

$$G_s = G_{s0}, G_c = G_{c0} + \frac{4V_{\text{in}}R_{\text{eq}}}{\pi L_eC_rX_{\text{eq}}\Omega_s^3}. \tag{37}$$

It is interesting to see that G_s and G_{s0} are consistent, whilst G_c is different from G_{c0}. The extra term in G_c reflects the interaction between the resonant inductor and the resonant capacitor.

Based on Fig. 9, the transfer function from $\hat{v}_{\text{in}}$ to $\hat{v}_{\text{o}}$, denoted as $G_{\text{vg}}(s)$, and the transfer function from $\hat{\omega}_{\text{s}}$ to $\hat{v}_{\text{o}}$, denoted as $G_{\text{vf}}(s)$ are derived, as seen in (38)(shown at the bottom of next page) and (39). They are still the three-order models and are of the same complexity compared to [20].

V. Noncoupled Equivalent Circuit

Note the proposed third-order equivalent circuit in Fig. 9 uses $\hat{i}_{\text{s}}$ and $\hat{i}_{\text{c}}$ as the state variables, which is inconvenient in practical use in that: $\hat{i}_{\text{s}}$ and $\hat{i}_{\text{c}}$ are coupled with each other; cand $\hat{i}_{\text{s}}$ and $\hat{i}_{\text{c}}$ are not the actual resonant current $\hat{i}_{\text{r}}$. Based on this consideration, this section intends to convert Fig. 9 to a new equivalent circuit with $\hat{i}_{\text{r}}$ being state variable.

The relationship between $\hat{i}_{\text{r}}$, $\hat{i}_{\text{s}}$ and $\hat{i}_{\text{c}}$ has been given in (25). According to (25), multiplying the voltage sources in the sine branch and cosine branch of Fig. 9 by $k_s\pi/2$ and $k_c\pi/2$, respectively, and then combining them together, the circuit with $\hat{i}_{\text{r}}$ as the state variable is obtained in Fig. 10. The voltage source $\hat{v}_{\text{x}}$ is a dependent voltage source expressed as

$$\hat{v}_x = \frac{\pi}{2}\left(k_sR_s\hat{i}_s + k_cR_y\hat{i}_s + k_cR_c\hat{i}_c - k_sR_x\hat{i}_c\right) \tag{40}$$

$\hat{v}_{\text{x}}$ needs to be eliminated so that the equivalent circuit can be more concise $\hat{v}_{\text{x}}$ is relevant to both $\hat{i}_{\text{r}}$ and the external excitaiton souces,$\hat{v}_{\text{in}}$ and $\hat{\omega}_{\text{s}}$, which will be analyzed separately below.

A. Relationship Between $\hat{v}_{\text{x}}$ and $\hat{i}_{\text{r}}$

Setting $\hat{v}_{\text{in}}$, $\hat{\omega}_{\text{s}}$ as zero in Fig. 8, we have

$$\begin{cases} R_x\hat{i}_c - \left(sL_e + R_s\right)\hat{i}_s = 2k_s\hat{v}_o \\ \left(sL_e + R_c\right)\hat{i}_c + R_y\hat{i}_s = -2k_c\hat{v}_o \end{cases}. \tag{41}$$

which is solved to be

$$\hat{i}_s = -\frac{4}{\pi}\frac{R_{\text{eq}}^2 - X_{\text{eq}}^2 + sL_eR_{\text{eq}}}{\sqrt{R_{\text{eq}}^2 + X_{\text{eq}}^2}\left(s^2L_e^2 + sL_eR_{\text{eq}} + X_{\text{eq}}^2\right)}\hat{v}_o \tag{42}$$

$$\hat{i}_c = \frac{4}{\pi}\frac{X_{\text{eq}}\left(sL_e + 2R_{\text{eq}}\right)}{\sqrt{R_{\text{eq}}^2 + X_{\text{eq}}^2}\left(s^2L_e^2 + sL_eR_{\text{eq}} + X_{\text{eq}}^2\right)}\hat{v}_o. \tag{43}$$

Substituting (42), (43) into (25) and (40), respectively,$\hat{i}_{\text{r}}$ and $\hat{v}_{\text{x}}$ and are obtained as

$$i_r = -\frac{4}{\pi}\frac{sL_e + R_{\text{eq}}}{s^2L_e^2 + sL_eR_{\text{eq}} + X_{\text{eq}}^2}\hat{v}_o \tag{44}$$

$$\hat{v}_x = -\frac{4}{\pi}\frac{X_{\text{eq}}^2}{s^2L_e^2 + sL_eR_{\text{eq}} + X_{\text{eq}}^2}\hat{v}_o \tag{45}$$

$\hat{v}_{\text{x}}$ divided by $\hat{i}_{\text{r}}$ leads to the following result,

$$\frac{\hat{v}_x}{\hat{i}_r} = \frac{X_{\text{eq}}^2}{sL_e + R_{\text{eq}}} \triangleq Z_x(s). \tag{46}$$

Obviously, $\hat{v}_{\text{x}}$ can be represented by an impedance Z_x when not considering the excitation sources. Furthermore, Z_x can be regarded as the parallel impedance of a capacitor C_e and a resistor R_e, as shown in Fig. 11. The values of C_e and R_e are

$$C_e = \frac{L_e}{X_{\text{eq}}^2}, R_e = \frac{X_{\text{eq}}^2}{R_{\text{eq}}}. \tag{47}$$

B. Relationship Between $\hat{v}_{\text{x}}$ and the Excitation Sources

When the controlled voltage source $\hat{v}_{\text{x}}$ is replaced with the impedance Z_x, the location of the external excitations, i.e., $\hat{v}_{\text{in}}$ and $\hat{\omega}_{\text{s}}$ will also alter. Both can be regarded as being composed of a voltage source in series with the inductor and a current source in parallel with the capacitor, as is shown in Fig. 12. The voltage source and the current source dependent on $\hat{v}_{\text{in}}$ are denoted as $K_{\text{v1}}\hat{v}_{\text{in}}$ and $K_{\text{v2}}\hat{v}_{\text{in}}$, respectively. The voltage source and the current source dependent on $\hat{\omega}_{\text{s}}$ are $K_{\text{f1}}\hat{\omega}_{\text{s}}$ and $K_{\text{f2}}\hat{\omega}_{\text{s}}$, respectively. From Fig. 12, the transfer function from $\hat{\omega}_{\text{s}}$ to $\hat{v}_{\text{o}}$ is

$$G_{\text{vf}}(s) = \frac{\frac{2}{\pi}R_{\text{Ld}}\left(K_{f2}X_{\text{eq}}^2 + K_{f2}R_{\text{eq}}^2 + sK_{f1}L_e\right)}{\left(1 + sC_oR_{\text{Ld}}\right)\left(s^2L_e^2 + sL_eR_{\text{eq}} + X_{\text{eq}}^2\right) + R_{\text{eq}}\left(R_{\text{eq}} + sL_e\right)}. \tag{48}$$

As (48) should be equal to (39), K_{f1}, K_{f2} are solved as

$$K_{f1} = \frac{4V_{\text{in}}R_{\text{eq}}}{\pi L_eC_r\Omega_s^3\sqrt{R_{\text{eq}}^2 + X_{\text{eq}}^2}} \tag{49}$$

$$K_{f2} = -\frac{4V_{\text{in}}\left(L_eL_r^2C_r^2\Omega_s^4 + C_rR_{\text{eq}}^2 - L_e\right)}{\pi L_eC_r^2X_{\text{eq}}^2\Omega_s^3\sqrt{R_{\text{eq}}^2 + X_{\text{eq}}^2}}. \tag{50}$$

Similarly, K_{v1}, K_{v2} are Solved to

$$K_{v1} = \frac{4R_{\text{eq}}}{\pi\sqrt{R_{\text{eq}}^2 + X_{\text{eq}}^2}}, K_{v2} = \frac{4}{\pi\sqrt{R_{\text{eq}}^2 + X_{\text{eq}}^2}}. \tag{51}$$

In comparison, K_{v1}, K_{v2} are consistent with the results in [20], whilst K_{f1}, K_{f2} are different. In particular, $K_{f1} = 0$ in [20] but is found to be non-zero here when considering the interaction between the resonant inductor and resonant capacitor.

VI. Discussion

This section will conduction a detailed analysis on the proposed model, including comparison with the exisitng model, dynmaic performance analysis, and sensitivity analysis.

A. Model Comparisons

Figs. 5 and 12 are, respectively, the equivalent circuit model by the existing literature [20] and this article. To facilitate comparison, all the differences between the two models are collectively given in Table V of Appendix Section, which shows two main distinctions, L_{e} and C_e are changed; and the voltage sources that relate to the frequency perturbation are different.

An SRC is designed to discuss the distinctions in detail. The circuit parameters of the SRC are given in Table I. The resonant frequency of the converter is 49.98 kHz.

Fig. 13 illustrates the bode diagrams of Gvg(s) from the simulation result, the existing equivalent circuit in [20], and the proposed equivalent circuit when the quality factor is 6.247. The switching frequencies of Figs. 13(a)–(c) are 29.98, 49.96, and 69.94 kHz, respectively. Hence, the beat frequency double poles for Fig. 13(a) and (c) are both 19.98 kHz. Obviously, the proposed equivalent circuit predicts the beat frequency dynamic more accurately. In contrast, the existing equivalent circuit in [20] deviates from the simulation even before the beat frequency double pole. This can be interpreted readily from the proposed equivalent circuit.

From Fig. 12, the resistor R_e functions like a dampling resistor of the C_e- L_e network. According to (47), when Ω_s gets far away from Ω_r, R_e becomes large, C_e is resonant with L_e, the resonant frequency being

$$\Omega_e = \frac{1}{2\pi\sqrt{L_eC_e}} = |\Omega_s - \Omega_r| \tag{52}$$

which is exactly the beat frequency double pole.

The bode diagrams of $G_{\text{vf}}(s)$ are presented in Fig. 14, where it is found that as Ω_s approaches Ω_r, the existing equivalent circuit in [20] has a significant deviation from the simulation in

$$G_{\text{vg}}(s) = \frac{\hat{v}_o(s)}{\hat{v}_{\text{in}}(s)} = \frac{R_{\text{eq}}}{\sqrt{R_{\text{eq}}^2 + X_{\text{eq}}^2}}\frac{\left(R_{\text{eq}}^2 + X_{\text{eq}}^2 + sL_eR_{\text{eq}}\right)}{\left(1 + sC_oR_{\text{Ld}}\right)\left(s^2L_e^2 + sL_eR_{\text{eq}} + X_{\text{eq}}^2\right) + R_{\text{eq}}\left(R_{\text{eq}} + sL_e\right)} \tag{38}$$

$$G_{\text{vf}}(s) = \frac{\hat{v}_o(s)}{\hat{\omega}_s(s)} = \frac{V_{\text{in}}R_{\text{eq}}\left(-\frac{\Omega_s^2+\Omega_r^2}{\Omega_s^2-\Omega_r^2}X_{\text{eq}}^2 + \frac{sR_{\text{eq}}}{C_r\Omega_s^2}\right)}{\Omega_s\sqrt{R_{\text{eq}}^2 + X_{\text{eq}}^2}\left[\left(s^2L_e^2 + sL_eR_{\text{eq}} + X_{\text{eq}}^2\right)\left(1 + C_oR_{\text{Ld}}s\right) + R_{\text{eq}}\left(sL_{\text{e}} + R_{\text{eq}}\right)\right]}. \tag{39}$$

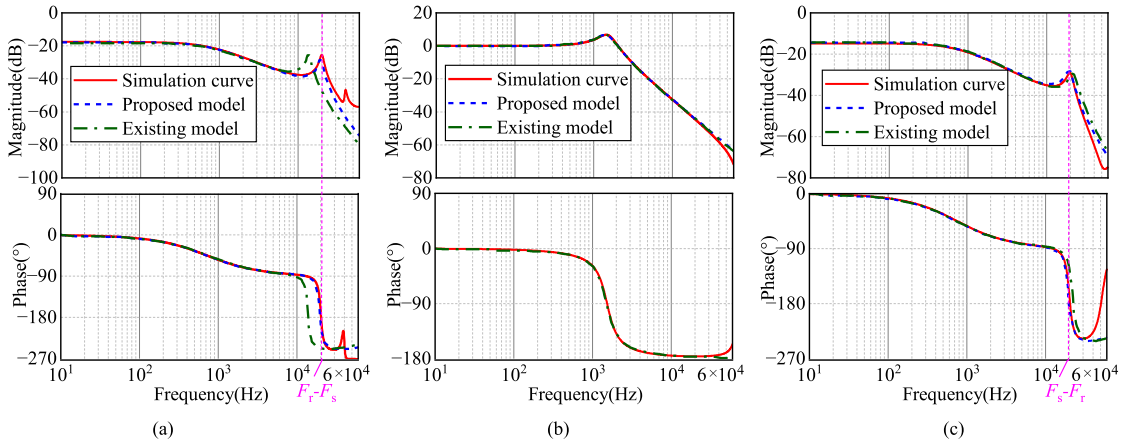

Fig. 13. Bode diagrams of G_{vg} when the quality factor $Q = 6.247$ at different switching frequencies. (a) $\Omega s = 0.6\ \Omega r$. (b) $\Omega s = \Omega r$. (c) $\Omega s = 1.4\ \Omega r$.

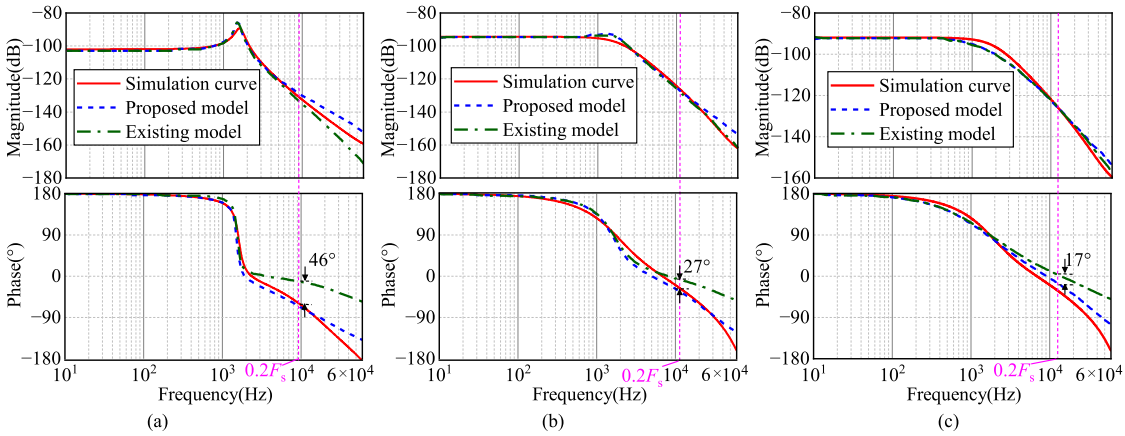

Fig. 14. Bode diagrams of Gvf when $Q = 0.521$ at different switching frequencies. (a) $\Omega s = 1.05\Omega r$. (b) $\Omega s = 1.15\ \Omega r$. (c) $\Omega s = 1.25\Omega r$.

TABLE II
PARAMETERS WHEN DOING DYNAMIC PERFORMANCE VERIFICATION

Parameter	Value	Parameter	Value
f_s	50.71 kHz	V_{in}	24 - 36 V
L_r	199 μH	C_o	33 μF
C_r	51 nF	R_{Ld}	7.75 - 31 Ω

the entire frequency range, while the proposed circuit is still able to track the simulation result very well. The phase prediction of the existing model in [20] is higher than the simulation phase, especially after $0.2F_s$, so closed loop design according to this model may lead to system instability, whereas the proposed model almost overlaps with the simulation model, reflecting that our model is more suitable for controller design. The phase issue can also be interpreted below from the proposed equivalent circuit.

When Ω_s approaches Ω_r, R_e approaches zero, the current source $K_{f2}\hat{\omega}_s$ is nearly short. Therefore, the effect of $\hat{\omega}_s$ is determined by $K_{f1}\hat{\omega}_s$. However, $K_{f1} = 0$ in [20], which means $\hat{\omega}_s$ has little effect on the circuit in the existing equivalent circuit in [20]. In particular, when $\Omega_s = \Omega_r$, $K_{f2}\hat{\omega}_s$ is absolutely short, the transfer function $G_{vf}(s) = 0$ in the existing equivalent circuit in [20], reaching a maximum error. As the bode diagram when $G_{vf}(s) = 0$ is infinitesimal, Ω_s is set at $1.05\Omega_r$ in Fig. 14(a)–(c) shows the characteristic when Ω_s approaches Ω_r. It can be found that the proposed model could capture the characteristics of the system up to about half of the switching frequency.

B. Model Dynamic Performance Analysis

To validate the model's dynamic prediction ability on various operating conditions, simulations were performed for both load step and input voltage step conditions, with simulation parameters as given in Table II. Simulation results (see Figs. 15 and 16) demonstrate that the proposed model accurately predicts the system's dynamic response under conditions where the load steps from 50% to 100% and the input voltage steps by ±20% . This conclusively establishes that the proposed model can precisely describe the system's dynamic characteristics across different operating conditions.

C. Model Sensitivity Analysis

To investigate the impact of key component parameter deviations on the performance of the proposed model, the sensitivity

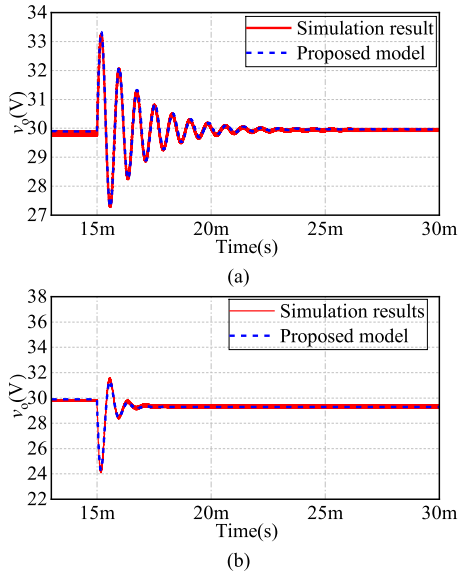

Fig. 15. Step responses when stepping the load resistance. (a) R_{Ld} steps from 15.5 to 31 Ω. (b) R_{Ld} steps from 15.5 to 7.75 Ω.

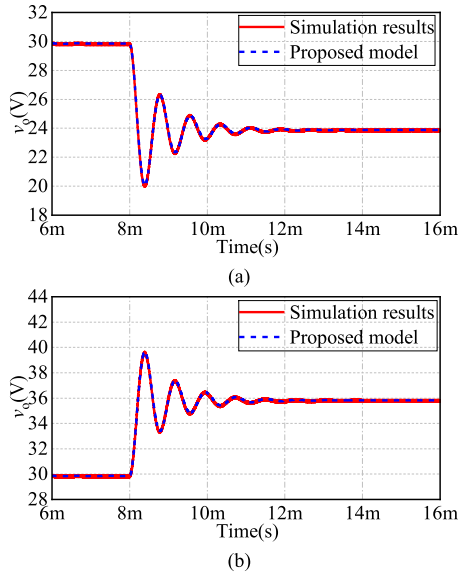

Fig. 16. Step responses when stepping the input voltage. (a) From 30 to 24 V. (b) From 30 to 36 V.

of G_{vg}, G_{vf} to L_r and C_r are analyzed. We define the normalized sensitivity as

$$S_x^y = \frac{\partial y/y}{\partial x/x} = \frac{x}{y}\frac{\partial y}{\partial x}. \tag{53}$$

The sensitivity of the proposed model transfer function G_{vg} with respect to L_r and C_r is given by

$$\begin{aligned} S_{L_r}^{G_{\mathrm{vg}}(s)} &= \frac{\partial G_{\mathrm{vg}}(s)}{\partial L_r}\frac{L_r}{G_{\mathrm{vg}}(s)} \\ S_{C_r}^{G_{\mathrm{vg}}(s)} &= \frac{\partial G_{\mathrm{vg}}(s)}{\partial C_r}\frac{C_r}{G_{\mathrm{vg}}(s)}. \end{aligned} \tag{54}$$

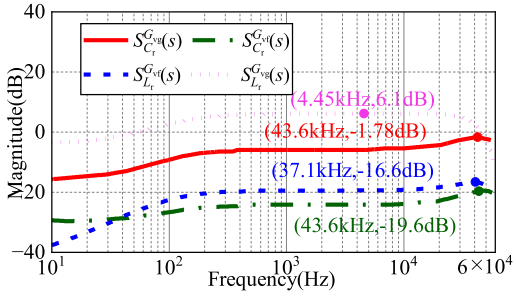

Fig. 17. Sensitivity of the transfer function to resonant components at the operating point of $fs = 2fr$ and $Q = 0.521$.

Considering the second-order terms, the sensitivity of the proposed model transfer function G_{vf} with respect to L_r and C_r is given by

$$\begin{aligned} S_{L_r}^{G_{\mathrm{vf}}(s)} &= \frac{\partial G_{\mathrm{vf}}(s)}{\partial L_r}\frac{\Delta L_r}{G_{\mathrm{vf}}(s)} + \frac{1}{2}\frac{\partial^2 G_{\mathrm{vf}}(s)}{\partial {L_r}^2}\frac{\Delta L_r^2}{G_{\mathrm{vf}}(s)} \\ S_{C_r}^{G_{\mathrm{vf}}(s)} &= \frac{\partial G_{\mathrm{vf}}(s)}{\partial C_r}\frac{\Delta C_r}{G_{vf}(s)} + \frac{1}{2}\frac{\partial^2 G_{\mathrm{vf}}(s)}{\partial {C_r}^2}\frac{\Delta C_r^2}{G_{\mathrm{vf}}(s)}. \end{aligned} \tag{55}$$

The magnitude characteristic is obtained as

$$\begin{aligned} A_{S_{L_r}^{G_{\mathrm{vf}}}}(s) &= 20\lg\left|S_{L_r}^{G_{\mathrm{vf}}}(s)\right| \\ A_{S_{C_r}^{G_{\mathrm{vf}}}}(s) &= 20\lg\left|S_{C_r}^{G_{\mathrm{vf}}}(s)\right|. \end{aligned} \tag{56}$$

Fig. 17 shows the normalized sensitivity curves of each transfer function to the resonant components under the operating condition of a switching frequency of 100 kHz and a quality factor $Q = 0.521$. As can be seen from the figure, the peak values of the four sensitivity curves, from top to bottom, are: 6.1 dB (corresponding to $S_{Lr}^{G\mathrm{vg}}$); −1.78 dB (corresponding to $|S_{Cr}^{G\mathrm{vg}}|$); −16.6 dB (corresponding to $|S_{Lr}^{G\mathrm{vf}}|$); and −19.6 dB (corresponding to $|S_{Cr}^{G\mathrm{vf}}|$).When the inductance value increases by 10% , the magnitudes of the transfer functions $|G_{\mathrm{vg}}(s)|$ and $|G_{\mathrm{vf}}(s)|$ exhibit deviations of 20.2% and 1.4% , respectively. When the capacitance value increases by 10% , the corresponding magnitudes of the transfer functions $|G_{\mathrm{vg}}(s)|$ and $|G_{\mathrm{vf}}(s)|$ exhibit deviations of 8.1% and 1.1% , respectively.

In this operating condition, the magnitude-frequency characteristic curves of $G_{\mathrm{vf}}(s)$ and $G_{\mathrm{vg}}(s)$ before and after a 10% increase in component parameters are shown in Fig. 18. To quantify the transfer functions' variation, the difference in function values before and after the parameter change is taken at the frequency corresponding to the maximum sensitivity. This difference in logarithmic coordinates is then converted to a linear value, thereby calculating the actual deviation. The results indicate that when the inductance value increases by 10% , the deviations of $|G_{\mathrm{vg}}(s)|$ and $|G_{\mathrm{vf}}(s)|$ are approximately 23.8% and 0, respectively. When the capacitance value increases by 10% , the deviations of the corresponding magnitudes of $|G_{\mathrm{vg}}(s)|$ and $|G_{\mathrm{vf}}(s)|$ are approximately 5% and 0, respectively. These results are consistent with the sensitivity calculations.

Under this condition, it can be observed that only $|G_{\mathrm{vg}}(s)|$ is sensitive to variations in L_r, while it remains insensitive to changes in C_r. In contrast, $|G_{\mathrm{vf}}(s)|$ shows negligible sensitivity

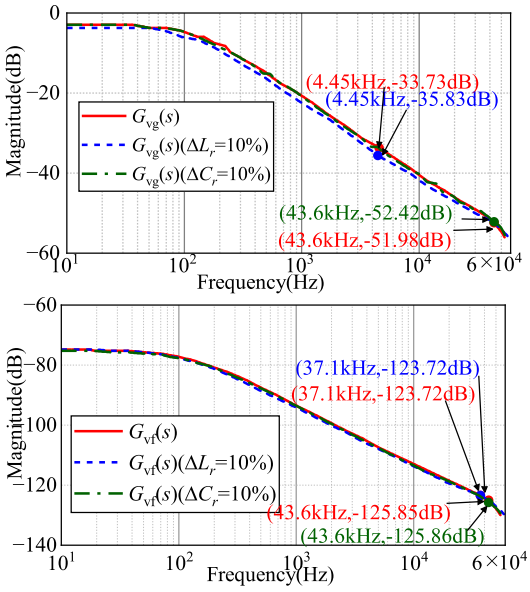

Fig. 18. Magnitude characteristic curves of Gvf(s) and Gvg(s) before and after a 10% increase in the values of the resonant components.

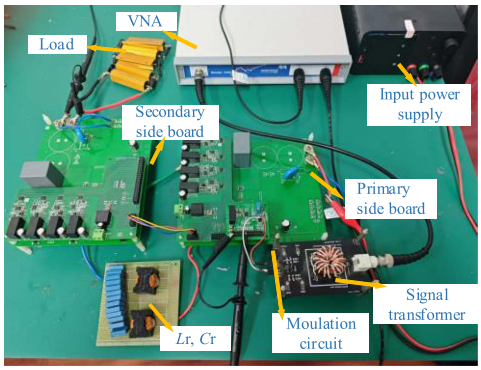

Fig. 19. Test platform for transfer function measurement.

to variations in both L_r and C_r. Please note that this analysis corresponds to the specific operating condition, for other conditions, sensitivity analysis should be performed again.

VII. Experimental Verification

The circuit parameters of the SRC are basically identical with Table I, except that the switching frequency and the Q value may change with the load. Prototype of the experimental circuit is shown in Fig. 19. It includes the main power circuit part and the transfer function measurement part. The main circuit part includes the primary-side bridge board, a secondary-side bridge board, the resonant network, and the load resistor. The transfer function measurement circuit includes the bode 100 network analyzer from Omicron, a signal isolation transformer, and a voltage-controlled oscillator (VCO) in UCC25600 to generate frequency perturbation.

Next, we will confirm the effectiveness of the model by measuring the transfer function and designing a closed-loop controller to observe stability.

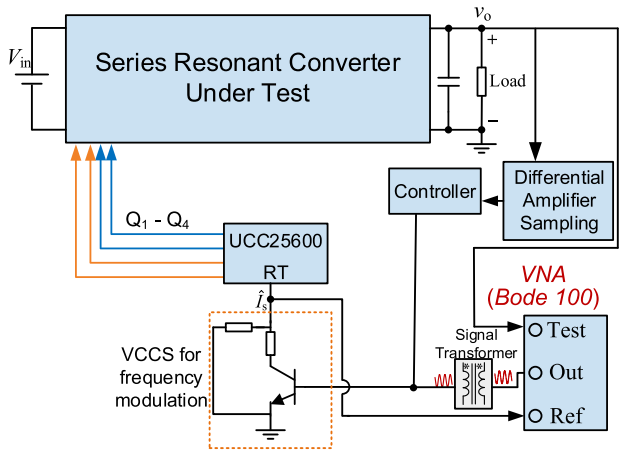

Fig. 20. Schematic diagram of the measurement of Gvf (s).

A. Measurement of the Transfer Function

The schematic diagram for measuring the transfer function $G_{\mathrm{vf}}(s)$ is demonstrated in Fig. 20. The measurement process initiates with Bode100 generating a sinusoidal sweep signal spanning frequency from 10 to 60 kHz. This signal undergoes galvanic isolation via a signal injection transformer, then is superimposed with offset current, which flows into a transistor-based voltage controlled current source to generate an amplified current for the inherent voltage controller oscillator of UCC25600. After that, the frequency of the generated driving signals for all switches. In this way, the frequency perturbation is realized. Then, the output voltage of the SRC is sent to the Test port of VNA after sampling. The frequency perturbation signal is sent to the Ref port. A transfer function that is the ratio of the test port signal to the Ref port signal is obtained. Calculating the dc gain K of the VCO, and dividing the transfer function obtained in the previous step by K leads to the final transfer function of $G_{\mathrm{vf}}(s)$.

Figs. 21 and 22 give the experimentally measured results of the of $G_{\mathrm{vf}}(s)$. The gain K is 78 dB in this case [18] and has been considered during the measurement.

It can be seen from Figs. 21 and 22 that the proposed equivalent circuit model coincides well with the experimental curve. The phase-frequency curve of this model is more consistent with experimental results than that of existing models, and the phase of the latter curve always leads that of the former curve. All these are consistent with the theoretical analysis.

B. Stability Evaluation by the Proposed Model

According to the previous analysis, the phase error of existing model in [20] gradually increases with the frequency, which will seriously affect the accuracy at high bandwidth control scenarios, and finally risk the stability of the system. To address this issue, two compensators of the closed-loop DABSRC system are designed here, with cut-off frequencies at $0.1F_{\mathrm{s}}$ (low bandwidth) and $0.2F_{\mathrm{s}}$ (high bandwidth), respectively. The block diagram illustrating the closed-loop control of the circuit is presented in Fig. 23, with $G_c(s)$ being the compensator and H_v being the gain

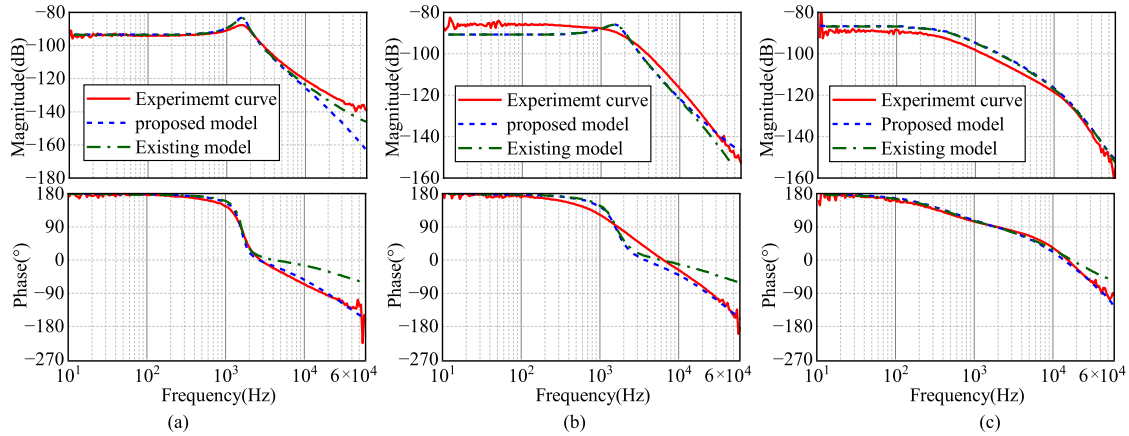

Fig. 21. Bode diagrams of Gvf(s) at different switching frequencies when $Q = 0.677$. (a) $\Omega s = 1.101\Omega r$. (b)$\Omega s = 1.114\ \Omega r$. (c) $\Omega s = 1.301\Omega r$.

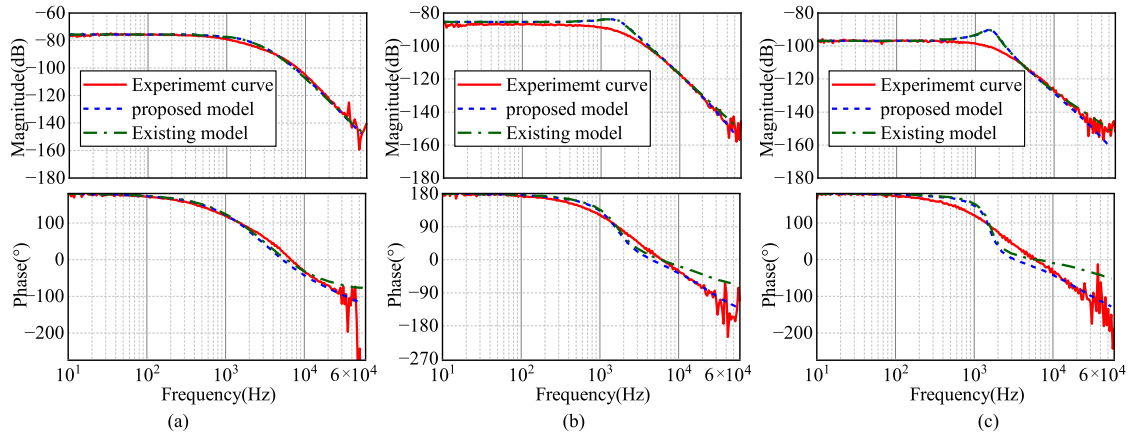

Fig. 22. Bode diagrams of Gvf(s) at different switching frequencies when $\Omega s = 1.101\Omega$r. (a) $Q = 2.082$. (b) $Q = 1.041$. (c) $Q = 0.521$.

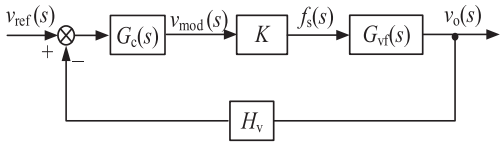

Fig. 23. Closed-loop control block diagram of the DABSRC system.

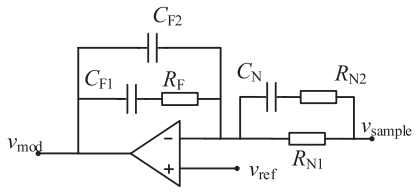

Fig. 24. Type III compensator.

TABLE III
TYPE III COMPENSATOR PARAMETERS AT LOW BANDWIDTH

Parameters	Values	Parameters	Values
H_v	0.02	R_F	27 kΩ
R_{N1}	10 kΩ	C_{F1}	56 nF
R_{N2}	43 Ω	C_{F2}	33 pF
C_N	47 nF	V_o	29.61 V

of the voltage sensor. The $G_c(s)$ is implemented with a type III compensator shown in Fig. 24. The loop gain of the closed-loop system is

$$T(s) = G_c(s)KG_{vf}(s)H_v. \tag{57}$$

The bode plots of $T(s)$ with different bandwidths are shown in Fig. 25. For the low-bandwidth case shown in Fig. 25(a), the compensation parameters are given in Table III. The cut-off frequency and phase margin predicted by the existing model are 6 kHz and 74.7°, while those of the proposed model are 5.7 kHz and 48.3°. According to the Nyquist criterion, both models predict the system to be stable. The experimental waveforms in Fig. 26 indicated that the system is actually stable, verifying that both models are useful at low bandwidth.

However, at high bandwidth, the conditions differ a lot. Fig. 25(b) displays the Bode plots of the corresponding T(s), with compensation parameters given in Table IV. It can be observed that the cut-off frequency and phase margin of the existing model are 11.3 kHz and 17.2°, while the proposed model are 14.1 kHz and −37.6°. According to the Nyquist criterion, the former case predicts stability, whereas the latter

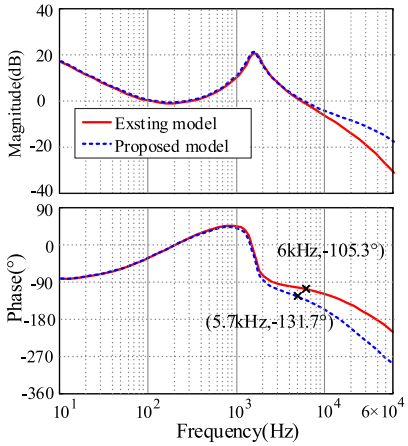

Fig. 25. Predicted bode plots of T(s) by both models at different bandwidths. (a) When the cut-off frequency is around $0.1F_s$. (b) when the cut-off frequency is around $0.2F_s$.

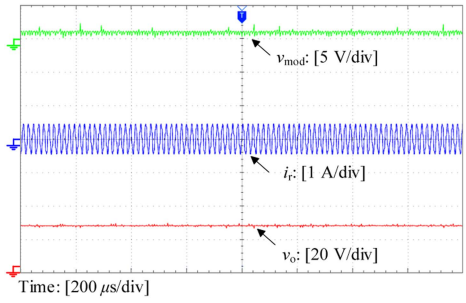

Fig. 26. Experimental waveforms with the cut-off frequency at $0.1F_s$, which is stable as predicted by both models.

TABLE IV
TYPE III COMPENSATOR PARAMETERS AT HIGH BANDWIDTH

Parameters	Values	Parameters	Values
H_v	0.02	R_F	910 kΩ
R_{N1}	10 kΩ	C_{F1}	1.8 nF
R_{N2}	750 Ω	C_{F2}	6 pF
C_N	2.7 nF	V_o	29.61V

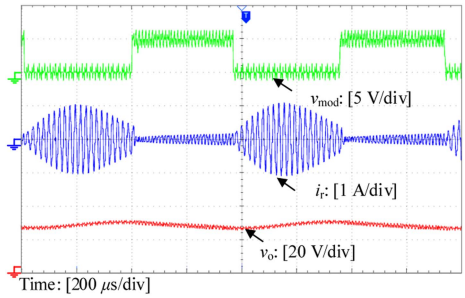

Fig. 27. Experimental waveforms with the cut-off frequency at $0.2F_s$, which is unstable as predicted by the proposed model.

predicts instability. The time-domain experimental waveforms presented in Fig. 27 shows that the system is in fact unstable. This validates that the proposed model is more accurate no matter the bandwidth is low or high, while existing models are only suitable for low-bandwidth design. It is worth noting that the proposed modeling is general and not limited to a specific controller type. As a result, it is applicable for guiding the design of various types of controllers, and contributes to a simpler, more reliable, and efficient controller design process.

VIII. CONCLUSION

This article proposed a third-order equivalent circuit of the SRC with the consideration of the interaction between the resonant inductor model and resonant capacitor model. The proposed equivalent circuit is concise in form. Fruitful physical insights are readily extracted from the derivation process of the model. Besides, the equivalent circuit shows good accuracy no matter when the switching frequency is above, below, or equal to the resonant frequency. The beat frequency dynamic is also explained using this equivalent circuit. Moreover, owing to its phase-frequency curve being more consistent with experiment, the proposed equivalent circuit model exhibits greater applicability in both low- and high-bandwidth closed-loop system design. Finally, the simulation and experimental results verify the validity of the new equivalent circuit model.

APPENDIX

The symbols associated with the fifth-order equivalent circuit of SRC [see Fig. 2(b)] are expressed as

$$k_{rs}=\frac{R_{\rm eq}^2X_{\rm eq}}{R_{\rm eq}^2+X_{\rm eq}^2},k_{rc}=\frac{R_{\rm eq}^2X_{\rm eq}}{R_{\rm eq}^2+X_{\rm eq}^2}$$
$$k_s=\frac{2}{\pi}\frac{R_{\rm eq}}{\sqrt{R_{\rm eq}^2+X_{\rm eq}^2}},k_c=-\frac{2}{\pi}\frac{X_{\rm eq}}{\sqrt{R_{\rm eq}^2+X_{\rm eq}^2}} \quad \text{(A1)}$$
$$R_s=\frac{R_{\rm eq}X_{\rm eq}^2}{R_{\rm eq}^2+X_{\rm eq}^2},R_c=\frac{R_{\rm eq}^3}{R_{\rm eq}^2+X_{\rm eq}^2}$$

TABLE V
COMPARISON BETWEEN THE EXISTING MODEL [20] AND THE PROPOSED MODEL

	Existing model in[20]	Proposed model
Equivalent inductance of the capacitor	$L_r\frac{\Omega_r^2}{\Omega_s^2}$	$L_r\frac{\Omega_r}{\Omega_s}$
Resonant network impedance	$\mathbf{Z}_{\mathrm{LC\_aprx}}(s)\approx sL_r\left(1+\frac{\Omega_r^2}{\Omega_s^2}\right)+jX_{eq}$	$\mathbf{Z}_{\mathrm{LC\_aprx0}}(s)\approx sL_r\left(1+\frac{\Omega_r}{\Omega_s}\right)+jX_{eq}$
Frequency perturbation coefficient(sin)	$G_s=-\frac{4V_{in}X_{eq}\left(1+\Omega_s^2L_rC_r\right)}{\pi C_r\Omega_s^2\left(R_{eq}^2+X_{eq}^2\right)}$	$G_s=-\frac{4V_{in}X_{eq}\left(1+\Omega_s^2L_rC_r\right)}{\pi C_r\Omega_s^2\left(R_{eq}^2+X_{eq}^2\right)}$
Frequency perturbation coefficient(cos)	$G_c=\frac{4V_{in}R_{eq}\left(1+\Omega_s^2L_rC_r\right)}{\pi C_r\Omega_s^2\left(R_{eq}^2+X_{eq}^2\right)}$	$G_{c0}=\frac{4V_{in}R_{eq}\left(1+\Omega_s^2L_rC_r\right)}{\pi C_r\Omega_s^2\left(R_{eq}^2+X_{eq}^2\right)}+\frac{4V_{in}R_{eq}}{\pi L_eC_rX_{eq}\Omega_s^3}$
Input-to-output transfer function	$G_{vg}(s)=\frac{\frac{R_{eq}}{\sqrt{R_{eq}^2+X_{eq}^2}}\left(R_{eq}^2+X_{eq}^2+sL_eR_{eq}\right)}{\left(s^2L_e^2+sL_eR_{eq}+X_{eq}^2\right)\left(1+C_oR_{Ld}s\right)+R_{eq}\left(sL_e+R_{eq}\right)}$	$G_{vg}(s)=\frac{\frac{R_{eq}}{\sqrt{R_{eq}^2+X_{eq}^2}}\left(R_{eq}^2+X_{eq}^2+sL_eR_{eq}\right)}{\left(s^2L_e^2+sL_eR_{eq}+X_{eq}^2\right)\left(1+C_oR_{Ld}s\right)+R_{eq}\left(sL_e+R_{eq}\right)}$
Frequency-to-output transfer function	$G_{vf}(s)=\frac{\frac{R_{eq}}{\sqrt{R_{eq}^2+X_{eq}^2}}\frac{V_{in}L_r^2}{\Omega_s^3}\left(\Omega_r^4-\Omega_s^4\right)}{\left(s^2L_e^2+sL_eR_{eq}+X_{eq}^2\right)\left(1+C_oR_{Ld}s\right)+R_{eq}\left(sL_e+R_{eq}\right)}$	$G_{vf}(s)=\frac{\frac{R_{eq}}{\sqrt{R_{eq}^2+X_{eq}^2}}\frac{V_{in}L_r^2}{\Omega_s^3}\left(\Omega_r^4-\Omega_s^4\right)\left[1+s\frac{R_{eq}\Omega_r^2}{L_r\left(\Omega_r^4-\Omega_s^4\right)}\right]}{\left(s^2L_e^2+sL_eR_{eq}+X_{eq}^2\right)\left(1+C_oR_{Ld}s\right)+R_{eq}\left(sL_e+R_{eq}\right)}$

$$V_s=-\frac{4V_{in}}{\pi\Omega_sC_r}\frac{X_{eq}}{R_{eq}^2+X_{eq}^2},V_c=-\frac{4V_{in}}{\pi\Omega_sC_r}\frac{R_{eq}}{R_{eq}^2+X_{eq}^2}$$
$$I_s=\frac{4V_{in}}{\pi}\frac{R_{eq}}{R_{eq}^2+X_{eq}^2},I_c=-\frac{4V_{in}}{\pi}\frac{X_{eq}}{R_{eq}^2+X_{eq}^2}. \tag{A2}$$

The symbols associated with the third-order equivalent circuit of SRC [see Fig. 4(b)] are expressed as

$$R_x=\frac{X_{eq}^3}{R_{eq}^2+X_{eq}^2},R_y=X_{eq}\frac{X_{eq}^2+2R_{eq}^2}{R_{eq}^2+X_{eq}^2}$$
$$G_{s0}=-\frac{4V_{in}X_{eq}\left(1+\Omega_s^2L_rC_r\right)}{\pi C_r\Omega_s^2\left(R_{eq}^2+X_{eq}^2\right)},$$
$$G_{c0}=\frac{4V_{in}R_{eq}\left(1+\Omega_s^2L_rC_r\right)}{\pi C_r\Omega_s^2\left(R_{eq}^2+X_{eq}^2\right)}. \tag{A3}$$

The symbols associated with the decoupled third-order equivalent circuit of SRC (see Fig. 5) are expressed as

$$K_{v0}=\frac{4}{\pi\sqrt{R_{eq}^2+X_{eq}^2}},K_{f0}=-\frac{4V_{in}}{\pi\Omega_s\sqrt{R_{eq}^2+X_{eq}^2}}\frac{\Omega_s^2+\Omega_r^2}{\Omega_s^2-\Omega_r^2}. \tag{A4}$$

When the output voltage is given, the corresponding switching frequency is known, (A5) shown at the bottom of this page.

The differences between [20] and the proposed model are given in Table V.

$$V_o=\frac{V_{in}\sin\left(\frac{\pi}{2}D_y\right)\Omega_sC_rR_{eq}}{\sqrt{\left(1-\Omega_s^2L_rC_r\right)^2+\left[\Omega_sC_r\left(R_{eq}+R_p\right)\right]^2}},\Omega_s=\sqrt{\frac{-\left\{\begin{array}{l}\left[C_r\left(R_{eq}+R_p\right)\right]^2\\-\left[\frac{V_{in}\sin\left(\frac{\pi}{2}D_y\right)C_rR_{eq}}{V_o}\right]^2-2L_rC_r\end{array}\right\}\pm\sqrt{\left\{\begin{array}{l}\left[C_r\left(R_{eq}+R_p\right)\right]^2\\-\left[\frac{V_{in}\sin\left(\frac{\pi}{2}D_y\right)C_rR_{eq}}{V_o}\right]^2-2L_rC_r\end{array}\right\}^2-4\left(L_rC_r\right)^2}}{2\left(L_rC_r\right)^2}}. \tag{A5}$$

REFERENCES

[1] Y. Zhang et al., "Integration of onboard charger and wireless charging system for electric vehicles with shared coupler, compensation, and rectifier," *IEEE Trans. Ind. Electron.*, vol. 70, no. 7, pp. 7511–7514, Jul. 2023, doi: 10.1109/TIE.2022.3204857.

[2] H. Vu and W. Choi, "A novel dual full-bridge llc resonant converter for cc and cv charges of batteries for electric vehicles," *IEEE Trans. Ind. Electron.*, vol. 65, no. 3, pp. 2212–2225, Mar. 2018, doi: 10.1109/TIE.2017.2739705.

[3] Y. Zhang, K. T., Z. Yan, Y. Mao, Z. Wu, and C. C. Mi, "Modeling and analysis of series-none compensation for wireless power transfer systems with a strong coupling," *IEEE Trans. Power Electron.*, vol. 34, no. 2, pp. 1209–1215, Feb. 2019, doi: 10.1109/TPEL.2018.2835307.

[4] Y. Wu, C. Liu, M. Zhou, X. Mao, and Y. Zhang, "An anti-offset electric vehicle wireless charging system based on dual coupled antiparallel coils," *IEEE Trans. Power Electron.*, vol. 38, no. 5, pp. 5634–5637, May 2023, doi: 10.1109/TPEL.2023.3238353.

[5] G. C. Verghese, M. E. Elbuluk, and J. G. Kassakian, "A general approach to sampled-data modeling for power electronic circuits," *IEEE Trans. Power Electron.*, vol. PE-1, no. 2, pp. 76–89, Apr. 1986, doi: 10.1109/TPEL.1986.4766286.

[6] J. Tang, S. Dong, C. Cui, and Q. Zhang, "Sampled-Data Modeling for Wireless Power Transfer Systems," *IEEE Trans. Power Electron.*, vol. 35, no. 3, pp. 3173–3182, Mar. 2020, doi: 10.1109/TPEL.2019.2928739.

[7] K. Siri, I. Batarseh, and C. Q. Lee, "Frequency response for the conventional parallel resonant converter based on the state-plane diagram," *IEEE Trans. Circuits Syst. I*, vol. 40, no. 1, pp. 33–42, Jan. 1993, doi: 10.1109/81.215343.

[8] Y. Hsieh and F. C. Lee, "Modeling resonant converters in a rotating, polar coordinate," in *Proc. IEEE Appl. Power Electron. Conf. Expo.*, 2018, pp. 938–943, doi: 10.1109/APEC.2018.8341127.

[9] S. R. Sanders, J. M. Noworolski, X. Z. Liu, and G. C. Verghese, "Generalized averaging method for power conversion circuits," *IEEE Trans. Power Electron.*, vol. 6, no. 2, pp. 251–259, Apr. 1991, doi: 10.1109/63.76811.

[10] H. Li, J. Fang, X. Li, S. Chen, and Y. Tang, "Modeling the dynamics of wireless power transfer using a generalized average model of high-Q resonators," in *Proc. IEEE Appl. Power Electron. Conf. Expo.*, 2018, pp. 3127–3130, doi: 10.1109/APEC.2018.8341547.

[11] H. Li, J. Fang, and Y. Tang, "Dynamic phasor-Based reduced-order models of wireless power transfer systems," *IEEE Trans. Power Electron.*, vol. 34, no. 11, pp. 11361–11370, Nov. 2019, doi: 10.1109/TPEL.2019.2897823.

[12] D. Seltzer, L. Corradini, D. Bloomquist, R. Zane, and D. Maksimovic, "Small signal phasor modeling of dual active bridge series resonant DC/DC converters with multi-angle phase shift modulation," in *Proc. IEEE Energy Convers. Congr. Expo.*, 2011, pp. 2757–2764, doi: 10.1109/ECCE.2011.6064139.

[13] E. X. Yang, B. Choi, F. C. Lee, and B. H. Cho, "Dynamic analysis and control design of LCC resonant converter," in *Proc. IEEE Power Electron. Specialists Conf.*, 1992, pp. 362–369, doi: 10.1109/PESC.1992.254651.

[14] Z. U. Zahid et al., "Modeling and control of series-series compensated inductive power transfer system," *IEEE J. Emerg. Sel. Topics Power Electron*, vol. 3, no. 1, pp. 111–123, Mar. 2015, doi: 10.1109/JESTPE.2014.2327959.

[15] E. X. Yang, "Extended describing function method for small-signal modeling of resonant and multi-resonant converters," Ph.D. dissertation, in *Dept. Elect. Comput. Eng.*, Blacksburg, VA, USA: Virginia Tech, Feb. 1994.

[16] E. X. Yang, F. C. Lee, and M. M. Jovanovic, "Small-signal modeling of series and parallel resonant converters," in *Proc. IEEE Power Electron. Specalists Conf.*, 1992, pp. 785–792.

[17] A. F. Witulski, A. F. Hernandez, and R. W. Erickson, "Small signal equivalent circuit modeling of resonant converters," *IEEE Trans. Power Electron.*, vol. 6, no. 1, pp. 11–27, Jan. 1991, doi: 10.1109/63.64999.

[18] C. T. Rim and G. H. Cho, "Phasor transformation and its application to the DC/AC analyses of frequency phase-controlled series resonant converters (SRC)," *IEEE Trans. Power Electron.*, vol. 5, no. 2, pp. 201–211, Apr. 1990, doi: 10.1109/63.53157.

[19] V. Vorperian, "Approximate small-signal analysis of the series and the parallel resonant converters," *IEEE Trans. Power Electron.*, vol. 4, no. 1, pp. 15–24, Jan. 1989, doi: 10.1109/63.21869.

[20] S. Tian, F. C. Lee, and Q. Li, "A simplified equivalent circuit model of series resonant converter," *IEEE Trans. Power Electron.*, vol. 31, no. 5, pp. 3922–3931, May 2016, doi: 10.1109/TPEL.2015.2464351.

[21] S. Vyapari, N. R. V., and G. Ghosh, "Envelope-detection-based accurate small-signal modeling of series resonant converters," *IEEE Trans. Power Electron.*, vol. 38, no. 7, pp. 8367–8378, Jul. 2023, doi: 10.1109/TPEL.2023.3268635.

[22] V. T. Chacko and N. Lakshminarasamma, "Modeling of series resonant converter in synchronous rotating frame," in *Proc. IEEE Int. Conf. Power Electron., Smart Grid, Renew. Energy*, 2022, pp. 1–6, doi: 10.1109/PESGRE52268.2022.9715898.